Quantitative phase imaging of adherent mammalian cells: a comparative study

C. Allier, L. Hervé, O. Mandula, P. Blandin, Y. Usson, J. Savatier, S. Monneret, S. Morales

Research Article | Vol. 10, No. 6 | 1 Jun 2019 | BIOMEDICAL OPTICS EXPRESS 2768
Biomedical Optics EXPRESS

Quantitative phase imaging of adherent mammalian cells: a comparative study

C. ALLIER,[1,*] L. HERVÉ,[1] O. MANDULA,[1] P. BLANDIN,[1] Y. USSON,[2] J. SAVATIER,[3] S. MONNERET,[3] AND S. MORALES[1]

[1] *Univ. Grenoble Alpes, CEA, LETI, DTBS-LSIV, F-38000 Grenoble, France*
[2] *TIMC-IMAG, Uni. Grenoble Alpes, CNRS UMR 5525, France*
[3] *Aix Marseille Univ, CNRS, Centrale Marseille, Institut Fresnel, Marseille, France*
[*] *cedric.allier@cea.fr*

Abstract: The quantitative phase imaging methods have several advantages when it comes to monitoring cultures of adherent mammalian cells. Because of low photo-toxicity and no need for staining, we can follow cells in a minimally invasive way over a long period of time. The ability to measure the optical path difference in a quantitative manner allows the measurement of the cell dry mass, an important metric for studying the growth kinetics of mammalian cells. Here we present and compare cell measurements obtained with three different techniques: digital holographic microscopy, lens-free microscopy and quadriwave lateral sheering interferometry. We report a linear relationship between optical volume density values measured with these different techniques and estimate the precisions of this measurement for the different individual instruments.

1. Introduction

In cell microscopy, quantitative phase imaging (QPI) [1,2] holds a special position. QPI allows monitoring of adherent cell cultures continuously over several days [3–6]. QPI images of adherent cells are highly contrasted and can be further processed to quantify cellular features, related to morphology, density, and texture [7,8]. Importantly, the pixel intensity of QPI image can be related to the optical path difference (OPD), which quantifies the integral of the sample object refractive index difference with respect to the surrounding medium along the optical path. In practice, this value is calculated via the measurement of the phase shift $\varphi_{shift}(x,y)$:

$$\begin{aligned} \varphi_{shift}(x,y) &= \varphi(x,y) - \varphi_{medium} \\ OPD(x,y) &= \lambda \frac{\varphi_{shift}(x,y)}{2\pi} = \int_0^h [n(x,y,z) - n_{medium}]\, dz \end{aligned} \tag{1}$$

where n is the local sample refractive index, n_{medium} is the surrounding medium refractive index, z is the position along the optical axis, h is the thickness of the sample object and λ is the illumination wavelength. If the phase measured in the sample-free area is not constant, e.g. if the acquisition presents slow spatial variation, a baseline image must be estimated to measure precisely the phase shift. The OPD values can be integrated over the total projected area S of the cell. Here we use the optical volume difference (OVD) denomination introduced in [9] to define this integral. It is expressed as a unit of volume in μm^3:

$$OVD = \int_S OPD(x,y)\, dx\, dy \tag{2}$$

A relationship between the phase shift measurement and the cell mass has been defined in [10,11] and can be used to convert OVD to cell dry mass (CDM) measurements, the mass of the cellular content except water. Under our notation, this relationship is simply given by:

$$CDM = \frac{OVD}{\alpha} \tag{3}$$

#349973 https://doi.org/10.1364/BOE.10.002768
Journal © 2019 Received 30 Nov 2018; revised 8 Mar 2019; accepted 11 Mar 2019; published 14 May 2019

Biomedical Optics EXPRESS

where α is the specific refractive increment which relates the refractive index change to increase in mass density. There is a variety of substances within a cell. However the specific refractive index of these substances falls with a narrow range and Barer [10] defined an α constant of $0.18\,\mu m^3.pg^{-1}$ for most eukaryotic cells, taking into account not only proteins, but also lipids, sugars, and nucleic acids. Note, that the specific refractive increment is valid for cells in water. In our study we measured fixed cell sample where the refractive index of embedding medium was unknown. Therefore we cannot translate our OVD values into cell dry mass according to Eq. (3). For this reason we use OVD as a quantity for the comparison measurements.

In this article, we present a comparison study of three different QPI techniques. We used three commercially available QPI instruments: digital holographic microscopy (DHM) [12], quadriwave lateral sheering interferometry (LSI) [13] and lens-free microscopy (LFM) [14–16]. To ensure consistency, the measurements with the different techniques were performed on the same day, in the same room and on the same set of cells. Each instrument was operated by a separated experienced team using this particular instrument on daily basis.

The statistical analysis of the data allows us to demonstrate a linear relationship between the measurements obtained with different techniques and estimate the precision of the OVD for each instrument. The precision can be decomposed in two terms: reproducibility and repeatability. While the repeatability of the instrument can be directly measured as a deviation of consecutive measurements on the same cell, the reproducibility is difficult to access. The latter is estimated in our experimental design taking into account the variability of measuring cells with different morphologies and positions in the field of view.

The present study is not an intrinsic comparison of different optical methods, since the instruments are based on different principles. The magnification, coherence of the source, detector type etc. cannot be matched. Nevertheless, this study brings together and compares for the first time the characteristics of different QPI methods, when measuring the exact same set of adherent mammalian cells. In the first place, this study is intended for biologists to help in experimental design using QPI. The choice of an optimal QPI method will depend on each particular experiment.

2. Material and methods

2.1. Optical setup

A simple scheme of the three different QPI techniques is shown in Fig. 1 with technical specifications in Table 1.

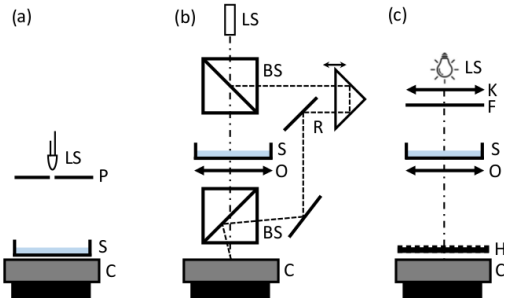

Fig. 1. Optical setups a) LFM b) DHM c) LSI. LS light source, P pinhole, S sample, C camera, O microscope objective, BS beam splitter, R variable length reference arm, K Kohler illumination system, F band-pass filter, H modified Hartmann mask. Note that light source is partially coherent for LSI (Kohler illumination), and LFM (LED with a pinhole) and coherent (laser) for DHM (b). Modified Hartmann mask H and camera C in (c) compose the Phasics camera mounted on a standard wide-field microscope.

Biomedical Optics EXPRESS

Table 1. Characteristics of the different optical setups used in this study.

Setup	Magnification	Numerical aperture	Image size	Number of pixels	Acquisition pixel pitch	Illumination wavelength
LFM	~0.97	/	27.7 mm^2	3840x2748	1.62 μm	647 nm
DHM	5×	0.12	1.2 mm^2	882x884	1.24 μm	668 nm
DHM	20×	0.7	0.075 mm^2	882x884	0.31 μm	668 nm
LSI	20×	0.5	0.244 mm^2	300x400	1.43 μm	>750 nm
LSI	40×	1.3	0.061 mm^2	300x400	0.71 μm	>750 nm

Lens-free microscopy (LFM)

Lens-free acquisitions were performed with a Cytonote microscope (Iprasense, Montpellier, France). This setup is inspired by the lens-free imaging system described in [17], which was modified to perform continuous monitoring of cellular cultures inside an incubator at a controlled temperature and humidity [15, 16]. Multiple wavelength illumination is provided by a RGB LEDs with red (647 nm, FWHM 13 nm), green (527 nm, FWHM 21 nm) and blue (450 nm, FWHM 15 nm) color. The light passes through a 50 μm pinhole at a distance of approximately 5 cm from the sample. The CMOS sensor is in contact with the cell culture recipient at a distance of ~1.5 mm (see Fig. 1(a)). The OPD reconstruction of the data at 647 nm from multiple wavelength acquisitions is based on constrained Fresnel propagation and is described in appendix A.1.

Digital holographic microscopy (DHM)

Digital holographic microscopy was performed using Lyncée tec DHM T-10105 (Lyncée Tec, Lausanne, Switzerland) with λ = 668nm laser light source. The object beam passes through the sample and is collected by an air objectives (5× 0.12NA and 20× 0.7NA). The variable-length reference beam is tilted to create an off-axis configuration (see Fig. 1(b)). The hologram resulting from the interference of the object and reference beams is recorded with a TXF14 CCD camera (Baumer-Optronic). Complex wavefields were reconstructed from the recorded holograms using a combination of the basic Fresnel transform and angular spectrum methods.

Lateral shearing interferometry (LSI)

The lateral shearing interferometry was performed on a conventional inverted microscope (Zeiss Observer Z1) with 20× 0.7NA air and 40× 1.3NA oil objective using Kohler illumination with a 750 nm long pass filter (AHF F32-750E). A wavefront sensor SID4Bio (Phasics, Saint-Aubin, France) was mounted on the video port of the microscope. The wavefront sensor SID4Bio contains a 2D grating (modified Hartmann mask) placed in front of the camera. The grating replicates the incident wavefront and after a short propagation an interferogram is recorded on a CCD camera (see Fig. 1(c)). The interferogram is analyzed in real time by Fourier transforms to extract intensity in 0 order and OPD gradients in 1 orders, along X and Y directions. The latter are finally integrated in two dimensions to yield wavefront measurement, which is the OPD in the projective approximation [13].

2.2. Fixed cells

COS-7 (fibroblast like, african green monkey kidney) cells were incubated at low density overnight on poly-L-lysin coated coverslips in 12 well plate, in DMEM (Gibco) supplemented with 10% FBS (Dutscher) and L-Glutamine. They were then rinsed with PBS and fixed with 2% glutaraldehyde for 10 minutes, then rinsed three times with PBS. They were quickly rinsed once

Biomedical Optics EXPRESS

with ultrapure water to avoid formation of salt crystals, then mounted on a slide with Fluoromount medium (Sigma). They were finally stored at 4°C before imaging.

2.3. Optical path difference measurements and post-processing

The measurements from the three different techniques were converted into OPD values (see Eq. (1)). Note, that the illumination wavelength differs between the different instruments (see table 1). In this article we neglect the chromatic dispersion of the refractive index in Eq. (1). A background estimated from a sample-free image was subtracted from all measurements. In addition, we used a custom-made iterative algorithm to estimate the residual low-frequency baseline (see appendix A.2). For each pair-wise comparison the images were re-scaled to have equal pixel-size (minimum of the two) with bicubic interpolation, rotated (bilinear interpolation) and co-registered. The scaling factor was determined by the ratio between the acquisition pixel pitches of the instrument calibrated with acquisitions of a USAF 1951 test chart (see Table 1) with an error estimated to three percents. The standard error of mean (s.e.m.) for the rotation angle determined from the registration of multiple different cells is below 0.5 degrees. The translation registration error is about 1 pixel, ($0.7 - 1.2\ \mu m$, depending on the instrument comparison). The registration errors are low, yet they will introduce a variability in the calculation of the OVD values. In order to diminish this source of error, in the case of manual ground truth segmentation, a best-matching algorithm is used to maximize the OVD value by slightly rotating and translating the manual mask with respect to the OPD map. Note, that the manual segmentation mask in the comparison was determined from the higher resolution image and applied to the rescaled and registrated lower resolution one. In the case of automatic cell segmentation, the mask is determined individually for each modality and the OVD value is slightly affected by the registration errors.

2.4. Experimental design and statistical approach

When determining the precision of OVD measurements of biological cells, we face the problem of the absence of the 'true' OVD values. Here we propose an experimental design with a statistical approach, which provides estimates of the OVD precision measurements in the absence of reference material.

The experimental design is based on the inter-modality comparisons of OVD measurements of a set of several tens of individual cells. Under the assumption of linear correlation of the measured OVD values with unknown true values OVD_T we set a simple model of the measurement with modality k and l:

$$\begin{cases} OVD_k = \alpha_k + \beta_k\, OVD_T + \epsilon_k \\ OVD_l = \alpha_l + \beta_l\, OVD_T + \epsilon_l \end{cases} \tag{4}$$

where ϵ_i is the noise term and α_i, β_i are the linear coefficients associated with modality i. Without the reference measurements of the true cell OVD_T values, it is impossible to extract the accuracy of each instrument, i.e. the difference between the true value and the measured value. However, by comparing a serie of cell OVD measurements obtained with different modalities, we can estimate the ratio β_l/β_k, the relative proportionality of the different QPI techniques. Further, we can determine the standard deviation of noise ϵ_i, which under our model defines the precision of the modality i. According to Eq. (4), we can define a linear relationship between the OVD values measured with two different modalities k and l:

$$OVD_l = \frac{\beta_l}{\beta_k} OVD_k + (\alpha_l - \frac{\beta_l}{\beta_k}\alpha_k) + (\epsilon_l - \frac{\beta_l}{\beta_k}\epsilon_k) \tag{5}$$

The fraction β_l/β_k can be estimated from the slope of the linear fit of the comparison measurements. From Eq. (5), we can calculate a variance of the residuals of the linear regression fit:

$$Var\left(OVD_l - \frac{\beta_l}{\beta_k} OVD_k\right) = Var(\epsilon_l) + \left(\frac{\beta_l}{\beta_k}\right)^2 Var(\epsilon_k) \tag{6}$$

Biomedical Optics EXPRESS

Substituting $Var\left(OVD_l - S_{l,k}\,OVD_k\right)$ by $\mathcal{V}_{l,k}$, β_l/β_k by $S_{l,k}$, $Var(\epsilon_k)$ by V_k and $Var(\epsilon_l)$ by V_l in Eq. (6) introduces the relationship between the variance V_l and V_k of the noise associated with individual modalities and the values $S_{l,k}$ (slope) and $\mathcal{V}_{l,k}$ (variance of the residuals) that can be both obtained experimentally:

$$\mathcal{V}_{l,k} = V_l + S_{l,k}^2 . V_k \tag{7}$$

In the present study, we considered five different modalities: LFM, DHM (with 5× and 20× objectives) and LSI (with 20× and 40× objectives), see Table 1. We choose to compare DHM and LSI with two different magnifications to determine the influence of the magnification on the precision of the instrument. Such an evaluation is not trivial since the magnification will affect not only the precision of the phase shift measurements but also the efficiency of the post-processing algorithm. With a large magnification, the cell segmentation algorithm will be more precise but the baseline subtraction can be worsened due to small background area. As such, we considered that an experimental evaluation was necessary. With five different modalities, we can make ten different comparisons. Eq. (7) leads to the following matrix equation:

$$\begin{bmatrix} 1 & S_{1,2}^2 & 0 & 0 & 0 \\ 1 & 0 & S_{1,3}^2 & 0 & 0 \\ 1 & 0 & 0 & S_{1,4}^2 & 0 \\ 1 & 0 & 0 & 0 & S_{1,5}^2 \\ 0 & 1 & S_{2,3}^2 & 0 & 0 \\ 0 & 1 & 0 & S_{2,4}^2 & 0 \\ 0 & 1 & 0 & 0 & S_{2,5}^2 \\ 0 & 0 & 1 & S_{3,4}^2 & 0 \\ 0 & 0 & 1 & 0 & S_{3,5}^2 \\ 0 & 0 & 0 & 1 & S_{4,5}^2 \end{bmatrix} \cdot \begin{bmatrix} V_1 \\ V_2 \\ V_3 \\ V_4 \\ V_5 \end{bmatrix} = \begin{bmatrix} \mathcal{V}_{1,2} \\ \mathcal{V}_{1,3} \\ \mathcal{V}_{1,4} \\ \mathcal{V}_{1,5} \\ \mathcal{V}_{2,3} \\ \mathcal{V}_{2,4} \\ \mathcal{V}_{2,5} \\ \mathcal{V}_{3,4} \\ \mathcal{V}_{3,5} \\ \mathcal{V}_{4,5} \end{bmatrix} \tag{8}$$

This equation is of the form $S \cdot V = \mathcal{V}$. If the condition number of the matrix S calculated with the slope values $S_{l,k}$ is low, then the problem associated with Eq. (8) is well posed and the variances of the noise terms associated with individual modalities can be estimated according to:

$$V = (S^T S)^{-1}(S^T \mathcal{V}) \tag{9}$$

The square root of the variance, the standard deviation $\sigma_i = \sqrt{V_i}$, gives the estimated precision of the OVD measurements for the different modalities. Note, that this method requires at least three different measurement, otherwise Eq. (8) is ill posed.

The errors margins on the estimated precisions can be evaluated numerically from simulated data of random OVD values with experimentally estimated parameters $S_{l,k}$ and ϵ_i drawn from a normal distribution with zero mean and variance V_i. We applied the methodology described above to this simulated dataset. The standard deviation of the estimated precision was calculated from N=1000 simulations. This estimated error margins take into account the uncertainty of the linear regression, which strongly depend on the number number of cell measurements per instrument comparison. The lower the number of experimental points, the larger the errors on the linear regressions and consequently the larger the errors on the precision estimations. In our experimental design the number of points per instrument comparison was chosen to be in the order of 100.

3. Results and discussion

3.1. Cell OPD map comparisons

Figure 2 shows the OPD map of two fixed COS-7 cells as acquired with different techniques, i.e. LFM, DHM(5× and 20×) and LSI(20× and 40×). There are some distinctive differences despite

Biomedical Optics EXPRESS

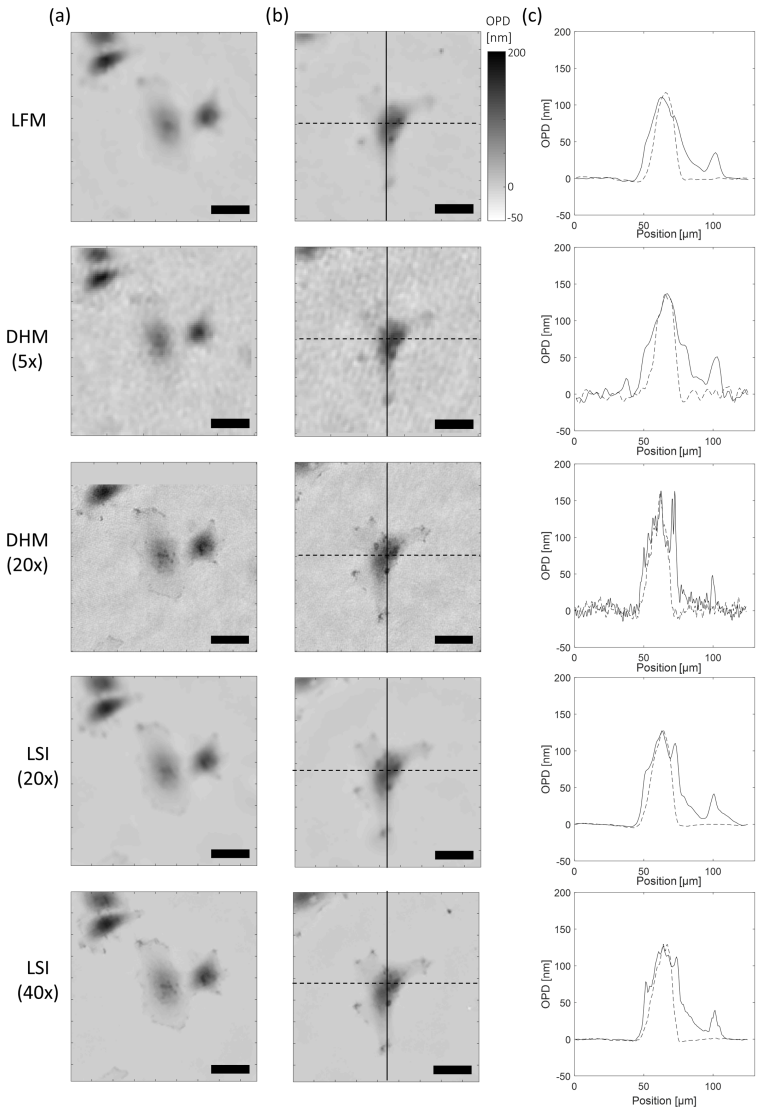

Fig. 2. (a, b) OPD maps of the same fixed COS-7 cells obtained with the different techniques. Scale bar is 25 μm. (c) OPD profiles measured through the cell center in (b) (solid line: vertical, dashed line: horizontal).

the overall similarity of the images. The OPD profiles are more or less smoothed with respect to the spatial resolution of the different techniques. Details on the micrometer scale are visible with LSI(40× and 20×) and DHM(20×), but are not resolved at lower magnification, i.e. with LFM and DHM(5×).

The OPD maps shown in Fig. 2 have been processed with a baseline subtraction algorithm (see sec. 2.3). Before baseline subtraction, the spatial variation of the background OPD values in a sample-free area of 50x50 μm^2 measured over several tens of images ranges between 2 and 9 nm depending on the instrument (see Fig. 3(g)). After baseline subtraction, the OPD values in sample-free areas are well centered around 0 nm for all modalities and the spatial variation ranges between ~1 nm (LFM and LSI) and ~3.5 nm (DHM) (see Fig. 3(g)).

Biomedical Optics EXPRESS

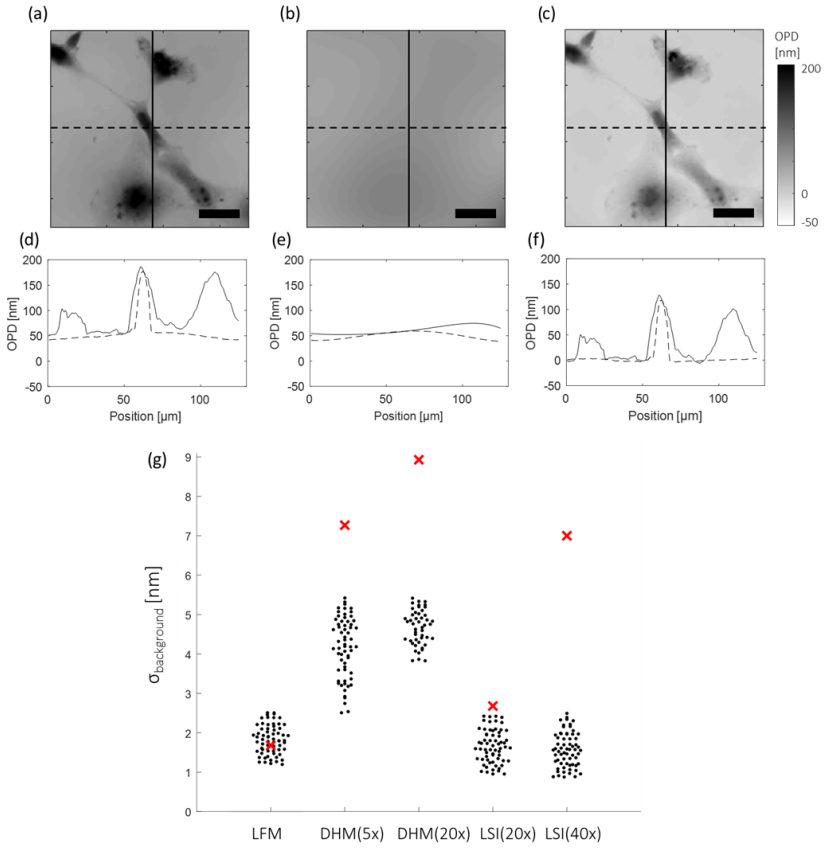

Fig. 3. Subtraction of the baseline image. (a) OPD raw map of a COS-7 cell (fixed) obtained by LSI(40×). (b) Estimation of the baseline image. (c) Final result after baseline subtraction, i.e. image(a)-image(b). Scale bar is 25 μm. (d, e, f) OPD profiles measured in the images (a, b, c) through the cell center (solid line: vertical, dashed line: horizontal). (g) The results of the baseline subtraction algorithm (black dots) are given by spatial variation measurements of the OPD values in sample-free area of 50x50 μm^2. The different points correspond to different parameters used in the baseline subtraction algorithm. One black dot depicts the average value over several tens of OPD map. The measurements before baseline subtraction are plotted with red crosses.

Figure 4(a,b) shows the OPD map of a fixed COS-7 cell obtained with LSI(40×) and LFM, respectively. There is a good correlation between the pixel to pixel comparison within the cell (Fig. 4(c), N=1491 pixels, coefficient of determination R^2=0.91, slope=0.91 and intercept=1.7 nm). By integrating the OPD values over the cell surface area determined on the LSI image with manual segmentation (Eq. (2)), we measured cell OVD in close agreement: 42.2 μm^3 for LSI(40×) and 40.9 μm^3 for LFM (see Fig. 4(a,b)). Registration error will influence the determination of the cell OVD value measured on the LFM acquisition. This error can be, however, reduced by a best-matching algorithm (see 2.3). Without the use of this algorithm the deviation of the OVD measurements related to registration error is about 0.18 μm^3 and is decreased to 0.03 μm^3 with the use of the best-matching algorithm (see Fig. 4(d)). A larger source of variability is in fact due to the baseline subtraction process (see appendix A.2) as shown in Fig. 4(e). The OVD values can vary by $\pm 1 \mu m^3$ (standard deviation) depending on the baseline subtraction algorithm parameters.

Biomedical Optics EXPRESS

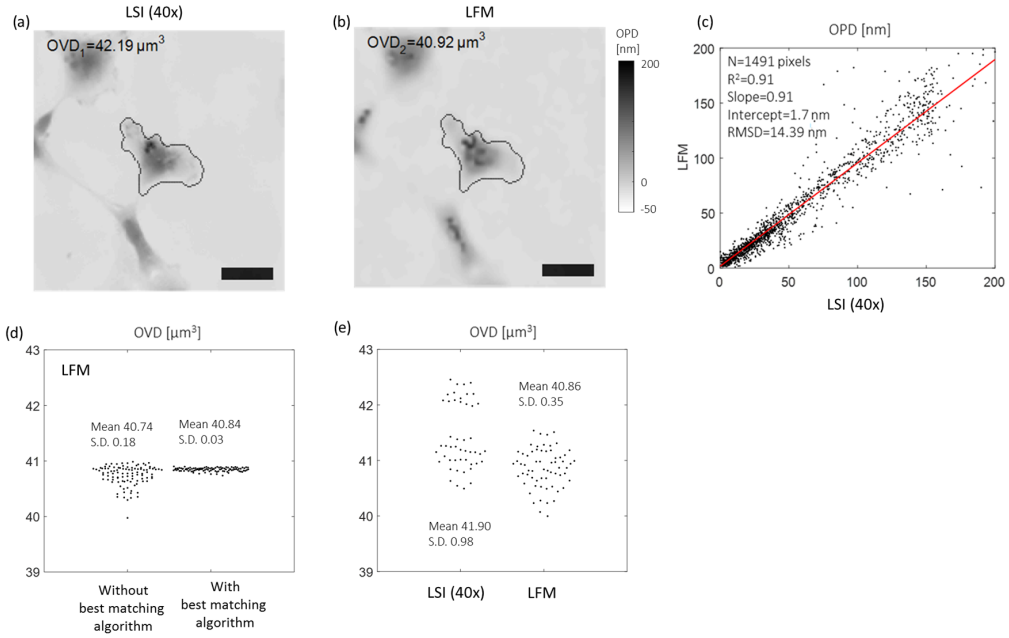

Fig. 4. Comparison between LSI(40×) and LFM. (a) OPD map of a fixed COS-7 cell obtained with LSI(40×). Scale bar is 25 μm. The contour of the ground truth cell segmentation area is shown in black. (b) OPD map obtained with LFM. (c) Pixel to pixel comparison between the OPD maps (within segmented cell area). The results of the linear regressions are indicated with values of slope, intercept, coefficient of determination (R^2) and root-mean-square deviation (RMSD). (d) OVD obtained with LFM when introducing registration errors of ±1 μm on the X-Y position and ±0.5 degree on the rotation. The results are shown with and without the use of the best-matching algorithm, which counterbalances these errors. (e) Plot of the cell OVD measurements for different baseline subtraction algorithm parameters.

3.2. *Estimation of the precision of the cell OVD measurements*

Figure 5 shows the pair-wise comparison of OVD for all different modalities measured over the same set of several tens of fixed COS-7 cells. First, we used manual ground truth cell segmentation and the baseline subtraction algorithm parameters which minimize the OPD spatial variation in the sample-free area (see Fig. 3(c)). Table 2 lists the results of the linear regression fitting for different cells (range between 5 and 100 μm^3). The slopes of the linear regressions are in the range of 0.83 to 1.02, the intercept values are in the range of −0.2 nm to 4.7 μm^3 and the coefficients of determination R^2 are all larger than 0.75.

These results indicate a good agreement between the different modalities for OVD measurement for fixed COS-7 cells. The OVD measurements obtained with LFM correlate linearly with the measurements obtained with DHM and LSI. It suggests that the present LFM setup can be considered as a QPI technique for the measurements of adherent cells. The values measured with LFM are systematically under-estimated by 10%. This is partly due to the sparsity constraints used in the holographic reconstruction algorithm (see appendix A.1).

The slopes values $S_{l,k}$ given in Table 2 were used to construct the matrix S in Eq. (8) and 9. The condition number of this matrix is 1.69, which means that the problem associated with Eq. (8) is well posed and the standard deviations $\sigma_i = \sqrt{V_i}$, the instruments precision, can be estimated via Eq. (9). The results of these calculations are given in Table 3. The estimated precisions range between 1.3 and 6 μm^3 and the error margins are estimated numerically, as described in sec. 2.4.

Biomedical Optics EXPRESS

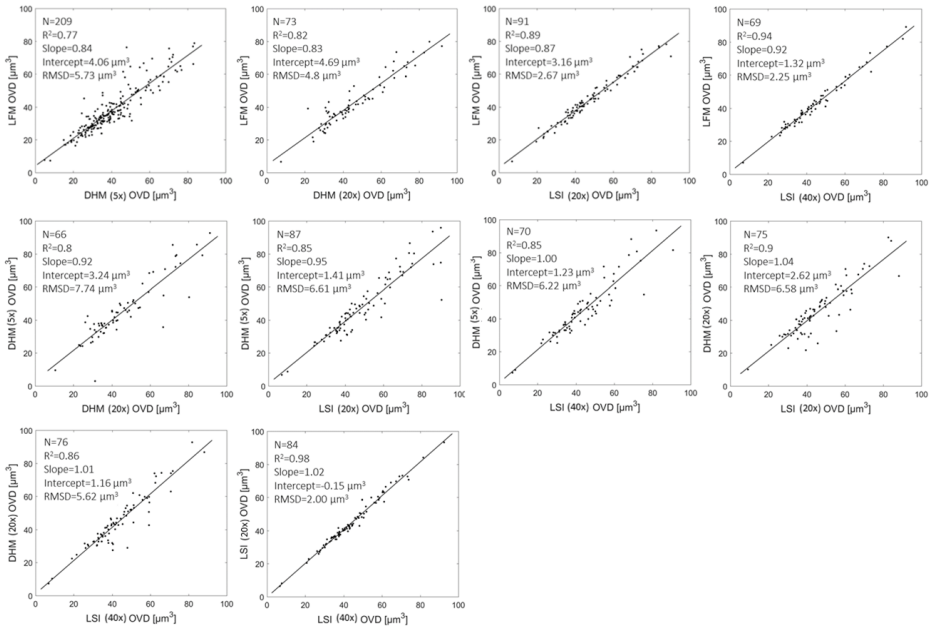

Fig. 5. Pair-wise comparisons of OVD measurements of fixed COS-7 cells. The OVD measurements are obtained with the ground truth cell segmentation and the baseline subtraction algorithm parameters which minimize the spatial variation in the sample-free area. The linear regression fitting curves are plotted in black. The results of the linear regressions are indicated with values of slope, intercept, coefficient of determination (R^2) and root-mean-square deviation (RMSD). N refers to the number of cell OVD measurements per comparison.

Table 2. Comparisons of the OVD measurements for fixed COS-7 cells.

l, k	Modality l	Modality k	N	$\mathcal{V}_{l,k}$ [μm^6]	Slope $S_{l,k}$	Intercept $I_{l,k}$ [μm^3]	RMSD [μm^3]	R^2
1,2	LFM	DHM(5×)	209	32.94	0.84	4.06	5.73	0.77
1,3	LFM	DHM(20×)	73	23.33	0.83	4.69	4.8	0.82
1,4	LFM	LSI(20×)	91	7.20	0.87	3.16	2.67	0.89
1,5	LFM	LSI(40×)	69	5.12	0.92	1.32	2.25	0.94
2,3	DHM(5×)	DHM(20×)	66	60.83	0.92	3.24	7.74	0.80
2,4	DHM(5×)	LSI(20×)	87	44.24	0.95	1.41	6.61	0.85
2,5	DHM(5×)	LSI(40×)	70	39.22	1.00	1.23	6.22	0.85
3,4	DHM(20×)	LSI(20×)	75	41.95	0.92	2.62	6.58	0.78
3,5	DHM(20×)	LSI(40×)	76	32.40	1.01	1.16	5.62	0.84
4,5	LSI(20×)	LSI(40×)	84	4.04	1.02	-0.15	2.00	0.98

N refers to the number of OVD measurements. The results of the linear regression fitting of the dataset of OVD_l and OVD_k: the slopes $S_{l,k}$, the intercept $I_{k,l}$, the variance term $\mathcal{V}_{l,k}$ (see Eq. (7)), the root-mean-squared-deviation (RMSD) and the coefficient of determination (R^2). The results are obtained with the ground truth cell segmentation and the baseline subtraction algorithm parameters which minimize the spatial variation in the sample-free area (see Fig. 3).

Biomedical Optics EXPRESS

Table 3. Results of the estimation of the standard deviations σ_i of the noise terms ϵ_i

	Estimated precision	LFM	DHM(5×)	DHM(20×)	LSI(20×)	LSI(40×)
1	$\sigma[\mu m^3]$	1.3±0.6	6.0±0.3	5.5±0.3	2.7±0.5	1.4±0.6
2	$\sigma[\mu m^3]$	1.9±0.2	3.8±0.2	3.1±0.2	0.8±0.3	1.2±0.4
3	$\sigma[\mu m^3]$	2.2±0.2	3.7±0.2	3.1±0.2	1.4±0.3	1.2±0.4

(1) Results obtained with manual ground truth cell segmentation and the baseline parameters which minimize the spatial variation in the sample-free area (see Fig. 3). (2) Results obtained with manual ground truth cell segmentation and optimized baseline subtraction algorithm parameters (see Fig. 7(a)). (3) Results obtained with an automatic seeded growing cell segmentation and the optimized baseline subtraction algorithm parameters.

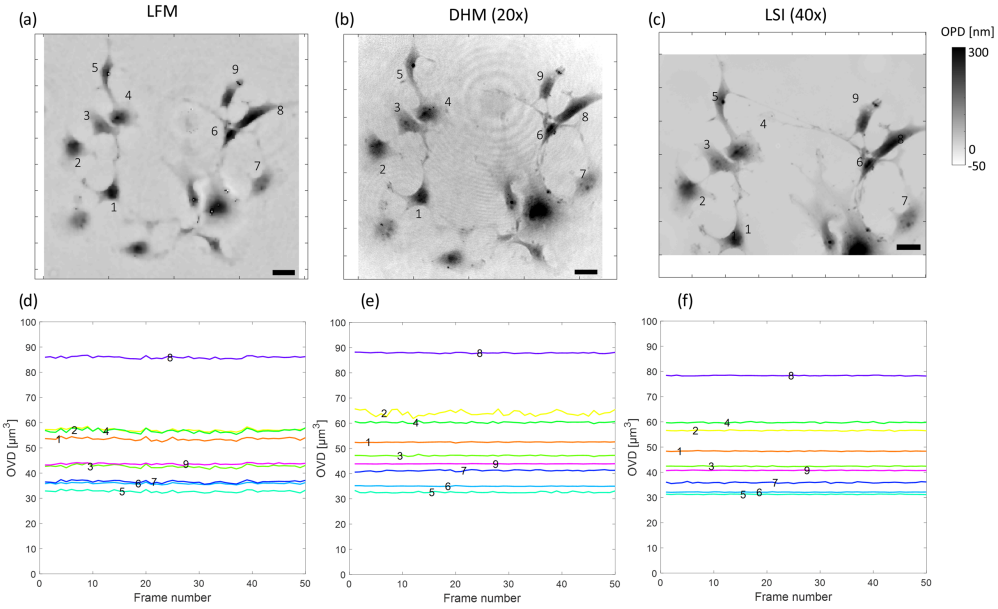

Fig. 6. (a, b, c) OPD image of fixed COS-7 cells obtained with (a) LFM, (b) DHM(20×) and (c) LSI(40×). The 9 cells of interest are numbered. (d, e, f) OVD measured on the 9 cells of interest over 50 consecutive acquisitions with LFM, DHM(20×) and LSI(40×).

The precision can be decomposed in two terms: reproducibility and repeatability. Repeatability can be directly measured as the deviation of consecutive measurements performed on the same cell in the same conditions as shown in Fig. 6. We measured OVD repeatability for nine different cells over 50 consecutive acquisitions. The deviation of the OVD values are 0.46 ± 0.13 μm^3 for LFM, 0.25 ± 0.27 μm^3 for DHM(20×) and 0.11 ± 0.05 μm^3 for LSI(40×). These values are low when compared to the estimated precision in Table 3. Reproducibility error is therefore the main contribution to the precision of OVD measurements. In our experimental design, the reproducibility errors accounts for the deviation of measuring cells with different geometries and positions in the field of view. Figure 7 shows the influence of baseline subtraction parameters on the estimation of the precision for different modalities. We found a common set of parameters for the baseline subtraction algorithm, which allowed us to get overall good precision with all modalities (see Fig. 7(a) and appendix A.2). The best precision 0.8 μm^3 is then obtained with LSI at magnification 20×. Increasing the magnification of LSI to 40× decreases slightly the precision to 1.2 μm^3. The precision of DHM was estimated to 3.8 μm^3 and 3.1 μm^3 for 5× and 20× magnifications, respectively. The precision of LFM was estimated at 1.9 μm^3.

Biomedical Optics EXPRESS

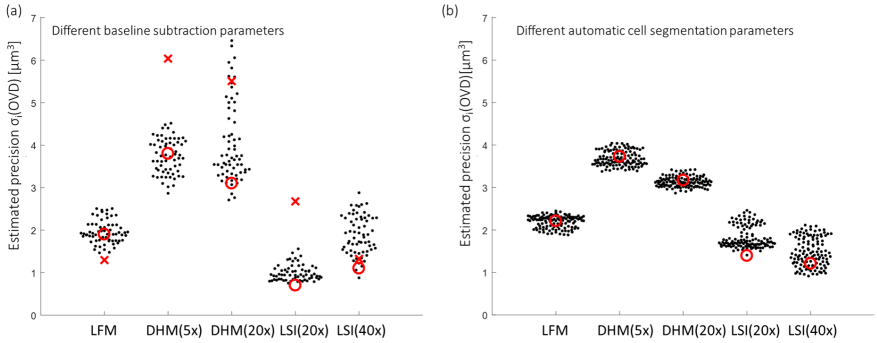

Fig. 7. Estimations of the instrument precisions. (a) Results obtained with manual ground truth cell segmentation. The different point correspond to different parameters used in the baseline subtraction algorithm, i.e. the sensitivity of the adaptive thresholding filter (ranging from 0.5 to 1), two different OPD threshold values (ranging from 2.5 nm to 12.5 nm) and the order of the polynomial fitting of the OPD values in sample-free area (ranging from 3 to 10). The red crosses point out the results obtained with the baseline subtraction algorithm which minimizes the spatial variation in the sample-free area (see Fig. 3). The results of the optimized baseline subtraction algorithm are shown with red circles (see appendix A.2). (b) Results obtained with automatic cell segmentation. The different points correspond to different threshold values used in the seeded growing segmentation algorithm ranging between 5 nm and 17.5 nm. The red circles correspond to the results obtained with threshold values of 10 nm for LFM, 12.5 nm for DHM and 5 nm for LSI.

A segmentation algorithm is necessary for automatic OVD measurement of a cell. Here we tested a seeded growing segmentation algorithm controlled by a single parameter, a threshold value which delineates the separation between the background and the cell area. The positions of the seeds were given manually. Fig. 8(a-c) shows the segmentation results for different OPD threshold values ranging from 0.5 to 25 nm. The difference between the automatic and the ground truth manual segmentation is given as intersection over union (IoU). Measuring the mean IoU value calculated over $N > 100$ cells as a function of the different threshold values is shown in Fig. 8(d). Maxima of IoU range between 0.65 and 0.8, depending on the modality. The automatic segmentation differs thus significantly from the ground truth, but remains in the range of the best segmentation results reported in the ISBI cell tracking challenge [18]. Figure 8(d) shows the mean ratio between the OVD measurements obtained with the automatic segmentation (OVD_{SEG}) and the ground truth segmentation (OVD_{GT}). A mean ratio superior to 0.9 can be obtained by setting the segmentation threshold values below 12.5 nm. The estimated precisions for different threshold values of the automatic cell segmentation algorithm are shown in Fig. 7(b). We found that the threshold values of 10 nm for LFM, 12.5 nm for DHM and 5 nm for LSI yield both good precision and large IoU. These threshold values correspond to ~5 times the spatial noise (see Fig. 3(g)). The estimated precisions, calculated with this post-processing parameters, range between 1.2 μm^3 and 3.7 μm^3 as shown in Table 3. These are slightly larger values than those obtained with manual segmentation (see Table 3). The automatic segmentation algorithm introduces significant errors in the determination of the cell surface area, but does not degrade the estimated precision too much. This is because the difference between the automatic and manual segmentation concerns pixels at the edges of the cell, where the OPD values are low. However, the accuracy, i.e. the difference between the true value and the measured value, is impacted since the measured OVD values are decreased by ~10% in comparison with the ground truth cell segmentation. To our knowledge, there is no report in the literature of precision measurements obtained with QPI for adherent cells. Previous reported results are consecutive

Biomedical Optics EXPRESS

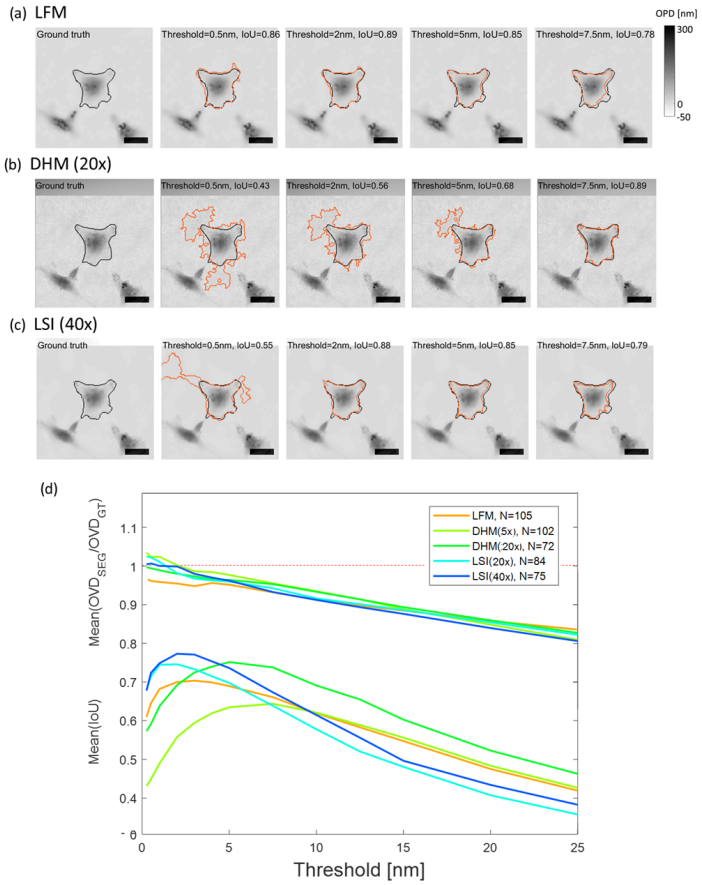

Fig. 8. (a-c) Automatic seeded growing segmentation of a fixed COS-7 cell as a function of the threshold parameter value. The contour of the automatic segmentation and the manual ground truth are overlaid in orange and black, respectively. (d) Plot of the mean IoU (intersection over union) value and the mean ratio between the OVD measurements obtained with the automatic segmentation (OVD_{SEG}) and the ground truth manual cell segmentation (OVD_{GT}) as a function of the segmentation threshold value for the different modalities.

measurements of the same cells estimating repeatability term only, which cannot be translated into precision. Reproducibility measurement on red blood cells using LSI is reported in [9]. Although these objects differ significantly from the adherent mammalian cells measured in this study, the reported precision of 0.8 μm^3 is comparable to our results. Considering non-optical mass profiling techniques, a precision of 8.5 pg measured on adherent cells have been obtained with resonant mass sensors [19]. This can be translated to OVD precision of 1.5 μm^3 according to Eq. (3). This is comparable with precision estimated for LSI (see Table 3).

4. Conclusion

The comparison between the three different QPI methods shows a good agreement when measuring cell OPD and OVD values. We estimated precision of the OVD measurements for different modalities from statistical analysis of pair-wise comparison measurements. The precision was in the range of 1 to 4 μm^3 depending on the modality for cell OVD values ranging between 10 and 100 μm^3. These precision values were achieved with finely adjusted parameters of the

Biomedical Optics EXPRESS

baseline subtraction and automatic segmentation algorithms. We show that the repeatability measurements that are often reported are only a minor contribution to the precision of each modality. We believe that the reported characteristics of different QPI methods will help to design and interpret biological experiments with cellular cultures involving QPI microscopy techniques.

A. Appendix

A.1. Lens-free holographic reconstruction

Contrary to conventional microscopy, LFM acquisitions are indirectly related to the sample. Therefore, specific numerical means are necessary to recover images from the sample optical properties. Contrary to DHM technique, the optical field is incompletely acquired by LFM setup since intensity measurements are insensitive to its phase. Such a lack of information leads to specific artifacts known as twin image in reconstructions [20]. To overcome this issue, priors are used in the reconstruction process in association with the use of multiple wavelength acquisitions. Besides, with the aim of being quantitative, partial coherence of the setup was taken into account. In the following we introduce the partially coherent forward model, we discuss the sample description and the optimization criterion. Finally we present the novel reconstruction procedure based on the above mentioned pieces of description.

A.1.1. Partially coherent forward model

Let consider the situation of a thin sample characterized by its complex-valued transmission $T_0(\vec{r},\lambda)$ at coordinate $\vec{r}$ in the sample plane and at wavelength λ. In this paper, the sample is illuminated by a set of three light fields corresponding to the use of the three colors of the RGB LED source. Let $c \in \{1,2,3\}$ be the index of the color. Let S^c be the sample illuminating light fields at color c. $S^c(\vec{r},\lambda,\vec{s})$ is the light field before the sample at wavelength λ, at position $\vec{r}$ in the sample plane regenerated by a source point located at position $\vec{s}$ in the source plane. The light field outgoing from the thin sample is:

$$A_0^c(\vec{r},\lambda,\vec{s}) = S^c(\vec{r},\lambda,\vec{s}).T_0(\vec{r},\lambda)$$

The Fresnel theory is used for describing the propagation of light for any peaked source point $(\vec{s},\lambda)$. At coordinate $\vec{r}\,'$ of the detector plane at distance Z from the sample, we have:

$$A_Z^c(\vec{r}\,',\lambda,\vec{s}) = \int d\vec{r}\; A_0^c(\vec{r},\lambda,\vec{s}).h_Z(\vec{r}\,'-\vec{r},\lambda) \tag{10}$$

with $h_Z(\vec{r},\lambda) = (1/i\lambda Z)\exp(i\pi\vec{r}^{\,2}/\lambda Z)$. For a given illuminating condition c, the measurement at the detector plane is the incoherent sum of the field A_Z^c. If the sensitivity of a pixel p is $D^p(\vec{r}',\lambda)$, intensity measurements I_Z are:

$$I_Z^{p,c} = \int d\vec{r}' \int d\vec{s} \int d\lambda\; D^p(\vec{r}',\lambda).\left|A_Z^c(\vec{r}\,',\lambda,\vec{s})\right|^2 \tag{11}$$

Such rigorous model takes into account the spatial partial coherence of the source related to the spatial extent of the source, the temporal partial coherence of the source related to the source spectra and the spatial discretization of the detector described by D^p. The two sources of partial coherence filter high frequencies of the measurements, and consequently creates a blurring of acquisitions. For transmission close to 1, we can prove that measurements can be more easily expressed by using a convolution kernel (K):

$$I_Z^{p,c} = W^c(\vec{r}_p).\left(\left|A_Z^c\right|^2 * K^c\right)_{\vec{r}_p} \tag{12}$$

where λ^c is the mean value of the c^{th} source spectrum, $A_Z^c(\vec{r}\,') \equiv A_Z(\vec{r}\,',\lambda_c)$ is the light field at the detector plan at wavelength λ^c, $\vec{r}_p$ is the position of the center of the pixel p and W is the "white" field which would be obtained from measurements in absence of sample. The kernels

Biomedical Optics EXPRESS

K^c can be numerically determined from simulation by computing $I_Z^{p,c}$ of Eq. (11) for a Dirac sample T_0. Such a simulation includes the spatial extent and the spectral width of the source through the choice of S^c; we used numerical values of section 2.1 for wavelengths, distances and spectral widths to determine K^c. Eq. (12) can be simply written as:

$$I_Z = W.\left(|T_0 * h_Z|^2 * K\right) \tag{13}$$

where pixel index p and color index c are understood. In practice, the transmission T_0 is discretized with the sampling of the setup detector as in [21] and the convolution product is perform in the Fourier domain knowing that the Fourier transform of h is $\tilde{h}_Z(\vec{\mu}, \lambda) = \exp(-i\pi\lambda Z\vec{\mu}^2)$, where the Fourier transform of a 2D function f is defined as: $\tilde{f}(\vec{\mu}) = \int d\vec{r}\ f(\vec{r}).\exp(-2i\pi\vec{\mu}.\vec{r})$.

A.1.2. Sample description

Optical Path Difference ($L^c(\vec{r})$) is used to describe the transmission properties $T_0^c(\vec{r})$ of the sample at wavelength λ^c and position $\vec{r}$ in the object plane:

$$T_0^c(\vec{r}) = A\exp\left(\frac{2i\pi L^c(\vec{r})}{\lambda^c}\right) \tag{14}$$

The variables L and A are the unknown real variable of the optimization problem. They are expected to have similar value along wavelength since the chromatic dispersion of the refractive index of biological samples is close the chromatic dispersion of water. The absorption A of the sample is assumed to be small since the biological samples used in this paper are not stained. A is low-pass filtered (with a kernel of 3×3 pixels) at every iteration.

A.1.3. Optimization criterion

The problem of the determination of the sample transmission with the LFM technique corresponds to a classical reconstruction problem aiming at producing a regular solution $L^{(\infty)}$, which measurement predictions M_Z (a function of implicit variable L) verify actual measurements $\overline{M_Z}$ at a good extent. In order to have at the same time, a regular object and good data matching, the next criterion is written:

$$\epsilon(L) = \epsilon_D(L) + \alpha.\epsilon_O(L) \tag{15}$$

The LFM result is the field $L^{(\infty)}$ which minimizes Eq. (15). As it will be discussed in part A.1.4, its minimization is tackled by an iterative method. ϵ_D in Eq. (15) measures the misfit between forward model predictions and actual measurements; since the variance of M_Z is constant, equal to $1/4$, the data matching term can be written as a χ^2 criterion:

$$\epsilon_D(L) = \frac{4}{N_p.N_c}\sum_c \int d\vec{r}\,'\ \left(M_Z^c(\vec{r}\,') - \overline{M_Z^c}(\vec{r}\,')\right)^2 \tag{16}$$

where N_p is the number of pixel of acquisition, N_c is the number of color (here $N_c = 3$) used and where for the sake of simplicity of the text, the symbol $\int d\vec{r}$ is used to replace the discrete summation: for any function f, such an integral replace: $\int d\vec{r} f(\vec{r}) \equiv \sum_p f(\vec{r}_p)$. The data matching term Eq. (16) is expected to reach the value of 1 for the solution.

The regularization term $\epsilon_O(L)$ of Eq.15 measures how regular an object field L is. In the case of the present paper, such a term was chosen as:

$$\epsilon_O(L) = \int d\vec{r}\left(\sqrt{\sum_c \varepsilon + \left(\left(\frac{\partial L^c(\vec{r})}{\partial x}\right)^2 + \left(\frac{\partial L^c(\vec{r})}{\partial y}\right)^2\right)} + \sqrt{\varepsilon + \sum_c \left(L^c(\vec{r})\right)^2} + 10.\left(\varepsilon + \sum_c \left(L^c(\vec{r}) < 0\right).\left(L^c(\vec{r})\right)^2\right)\right) \tag{17}$$

where $(L < 0)$ is a function which takes value 1 when $L < 0$ and 0 otherwise, where ε is a small positive real number (here 10^{-4}) used to make the quantities differentiable and to prevent division by 0 in following discussion (expression of the gradient of ϵ). The first term of Eq. (17) is a total variation term; it implements the preference for solution with sharp edges colocalized along the

Biomedical Optics EXPRESS

3 colors c. The second term of Eq. (17) is a L_1 term which lead to solutions with background region null valued thus promotes sparsity of solutions. The last term implements the preference for positive solution L in a soft manner. The three scalar coefficients of the three terms, i.e. 1, 1 and 10 are heuristically chosen weighting factors. The weighting factor α of Eq. (15) is used to balance data matching ϵ_D and regularization ϵ_O. Its choice is not trivial and is often discussed in the literature. Here, to tackle this problem of choice, α is made variable along optimization iterations. Since ϵ_D is expected to tend to 1, at iteration k, we take $\alpha^{(k)} = 1/\epsilon_O(L^{(k-1)})$ so as to produce automatic balancing of Eq. (15). To perform the optimization process as discussed in part A.1.4, the gradient of ϵ, $\nabla\epsilon = \nabla\epsilon_D + \alpha.\nabla\epsilon_O$ is needed. By using similar mathematical derivation as in [22], we find:

$$\nabla\epsilon_D^c(\vec{r}) = \frac{16\pi}{N_p.N_c} Im\left(\left(\left(\left(\left(W^c.\left(1-\frac{\overline{M_Z^c}}{M_Z^c}\right)\right)*K^c\right).A_Z^c\right)*h_{-Z}^c\right)_{\vec{r}}.A_0^c(\vec{r})^*\right) \tag{18}$$

We also find,

$$\nabla\epsilon_O^c(\vec{r}) = -\frac{\partial}{\partial x}\left(\frac{1}{e_1(\vec{r})}\frac{\partial L^c(\vec{r})}{\partial x}\right)\delta L^c(\vec{r}) - \frac{\partial}{\partial y}\left(\frac{1}{e_1(\vec{r})}\frac{\partial L^c(\vec{r})}{\partial y}\right) + \frac{L^c(\vec{r})}{e_2(\vec{r})} + 10.\left(L^c(\vec{r})<0\right).L^c(\vec{r}) \tag{19}$$

where $e_1(\vec{r}) = \sqrt{\sum_c \varepsilon + \left(\left(\frac{\partial L^c(\vec{r})}{\partial x}\right)^2 + \left(\frac{\partial L^c(\vec{r})}{\partial y}\right)^2\right)}$ and $e_2(\vec{r}) = \sqrt{\varepsilon + \sum_c \left(L^c(\vec{r})\right)^2}$. The gradient allows to compute variation $\delta\epsilon$ of the criterion ($\epsilon(L)$) for a small variation δL of the variable:

$$\delta\epsilon = \sum_c \int d\vec{r}\ \ \nabla\epsilon^c(\vec{r}).\delta L^c(\vec{r}) \tag{20}$$

A.1.4. Reconstruction procedure

The solution L^∞ of the LFM technique is obtained by minimizing iteratively the criterion Eq. (15) with the non-linear conjugate gradients method as described by the following pseudocode:

1/ initialization $k \leftarrow 0$, $D^{(k)} \leftarrow 0$, $L^{(k)} \leftarrow 0$
2/ $k \leftarrow k+1$
3/ computation of gradient $\nabla\epsilon^{(k)}$, of advancement direction $D^{(k)}$ and advancement step $\sigma^{(k)}$
4/ phase update: $L^{(k)} \leftarrow L^{(k-1)} + \sigma^{(k)}.D^{(k)}$
5/ test of convergence, if not reached go back to 2/

For step 3/, the gradient $\nabla\epsilon^{(k)}$ is analytically computed as detailed in section A.1.3. As discussed in the same section, parameter α varies with the iteration k to balance data matching and regularization terms. The advancement direction $D^{(k)}$ is obtained by conjugating the gradient $\nabla\epsilon^{(k)}$ with the previous direction of advancement $D^{(k-1)}$, using Hestenes-Stiefel formula [23]. The advancement step $\sigma^{(k)}$ (a scalar) is obtained by developing the criterion $\epsilon(L^{(k)} + \sigma.D^{(k)}) = f(\sigma)$ at order 2 with σ (Hessian computation) and by minimizing the resulting second-order polynomial. For the test of step 5/, we simply stop the algorithm when the number of iterations reaches 200.

A.2. Iterative algorithm for baseline subtraction

In every image, the algorithm segments the individual cells and determines the background region. The baseline is estimated from a polynomial fit of the background region. The baseline corrected image is then re-used to refine the segmentation of the individual cells and the process is repeated in three iterations with different segmentation algorithm in each iteration: in the first iteration we used adaptive threshold filter, in the second iteration a seeded growing segmentation algorithm and in the third iteration a simple thresholding filter. This baseline subtraction algorithm is thus parameterized with four parameters, i.e the order of the polynomial fitting, the sensitivity of the adaptive threshold, the threshold value of the seeded growing segmentation algorithm and the simple filter threshold value.

The best settings for different modalities is the following: sensitivity of the adaptive thresholding filter is set to 0.5, the threshold value of the seeded growing segmentation algorithm

Biomedical Optics EXPRESS

is set to 10 nm, the simple filter threshold is set to 7.5 nm and the order of the polynomial fitting to 9.

Disclosures

C. Allier and L. Hervé are inventors of a patent devoted to the holographic reconstruction. LSI as a QPI technique has been developed by J. Savatier and S. Monneret thanks to a close scientific collaboration with Phasics company.

References

1. M. Mir, B. Bhaduri, R. Wang, R. Zhu, and G. Popescu, "Quantitative phase imaging," Prog. Opt. **57**, 133–217 (2012).
2. Y. Park, C. Depeursinge, and G. Popescu, "Quantitative phase imaging in biomedicine," Nat. Photonics **12**, 578 (2018).
3. J. Reed, J. Chun, T. A. Zangle, S. Kalim, J. S. Hong, S. E. Pefley, X. Zheng, J. K. Gimzewski, and M. A. Teitell, "Rapid, massively parallel single-cell drug response measurements via live cell interferometry," Biophys. journal **101**, 1025–1031 (2011).
4. M. Mir, Z. Wang, Z. Shen, M. Bednarz, R. Bashir, I. Golding, S. G. Prasanth, and G. Popescu, "Optical measurement of cycle-dependent cell growth," Proc. Natl. Acad. Sci. **108**, 13124–13129 (2011).
5. G. Popescu, Y. Park, N. Lue, C. Best-Popescu, L. Deflores, R. R. Dasari, M. S. Feld, and K. Badizadegan, "Optical imaging of cell mass and growth dynamics," Am. J. Physiol. Physiol. **295**, C538–C544 (2008).
6. S. Monneret, P. Bon, G. Baffou, P. Berto, J. Savatier, S. Aknoun, and H. Rigneault, "Quadriwave lateral shearing interferometry as a quantification tool for microscopy. application to dry mass determination of living cells, temperature mapping, and vibrational phase imaging," in *Optical Methods for Inspection, Characterization, and Imaging of Biomaterials,* vol. 8792 (International Society for Optics and Photonics, 2013), p. 879209.
7. P. Bon, J. Savatier, M. Merlin, S. Monneret, and B. F. Wattellier, "Optical detection and measurement of living cell morphometric features with single-shot quantitative phase microscopy," J. Biomed. Opt. **17**, 076004 (2012).
8. M. Hejna, A. Jorapur, J. S. Song, and R. L. Judson, "High accuracy label-free classification of single-cell kinetic states from holographic cytometry of human melanoma cells," Sci. reports **7**, 11943 (2017).
9. S. Aknoun, J. Savatier, P. Bon, F. Galland, L. Abdeladim, B. F. Wattellier, and S. Monneret, "Living cell dry mass measurement using quantitative phase imaging with quadriwave lateral shearing interferometry: an accuracy and sensitivity discussion," J. biomedical optics **20**, 126009 (2015).
10. R. Barer, "Interference microscopy and mass determination," Nature **169**, 366 (1952).
11. H. Davies and M. Wilkins, "Interference microscopy and mass determination," Nature **169**, 541 (1952).
12. P. Marquet, B. Rappaz, P. J. Magistretti, E. Cuche, Y. Emery, T. Colomb, and C. Depeursinge, "Digital holographic microscopy: a noninvasive contrast imaging technique allowing quantitative visualization of living cells with subwavelength axial accuracy," Opt. letters **30**, 468–470 (2005).
13. P. Bon, G. Maucort, B. Wattellier, and S. Monneret, "Quadriwave lateral shearing interferometry for quantitative phase microscopy of living cells," Opt. express **17**, 13080–13094 (2009).
14. S. Seo, T.-W. Su, D. K. Tseng, A. Erlinger, and A. Ozcan, "Lensfree holographic imaging for on-chip cytometry and diagnostics," Lab on a Chip **9**, 777–787 (2009).
15. C. Allier, R. Vincent, F. Navarro, M. Menneteau, L. Ghenim, X. Gidrol, T. Bordy, L. Hervé, O. Cioni, S. Bardin *et al.*, "Lens-free video microscopy for the dynamic and quantitative analysis of adherent cell culture." J. visualized experiments: JoVE **132**, e56580 (2018).
16. C. Allier, S. Morel, R. Vincent, L. Ghenim, F. Navarro, M. Menneteau, T. Bordy, L. Hervé, O. Cioni, and X. Gidrol, "Imaging of dense cell cultures by multiwavelength lens-free video microscopy," Cytom. Part A **91**, 433–442 (2017).
17. T.-W. Su, S. Seo, A. Erlinger, and A. Ozcan, "High-throughput lensfree imaging and characterization of a heterogeneous cell solution on a chip," Biotechnol. bioengineering **102**, 856–868 (2009).
18. A. Muñoz Barrutia, S. Wolf, R. Mikut, C. C. Reyes-Aldasoro, H. M. Blau, L. Malmström, S.-Y. Cho, V. Ulman, P. Matula, F. Jug, M. Kozubek, E. Meijering, P. Quelhas, O. Dzyubachyk, J.-C. Olivo-Marin, F. a. Hamprecht, T. Esteves, J. Jaldén, D. Svoboda, M. Maška, O. Ronneberger, R. Bensch, T. Brox, P. Tomancak, J. a. Solis-Lemus, C. Haubold, A. C. Dufour, P. Matula, B. Lelieveldt, J. Stegmaier, C. Ortiz-de Solorzano, O. Demirel, Y. Li, I. Smal, N. Harder, K. Rohr, K. E. G. Magnusson, P. Xiao, and M. Radojevic, "An objective comparison of cell-tracking algorithms," Nat. Methods **14**, 1141–1152 (2017).
19. K. Park, L. J. Millet, N. Kim, H. Li, X. Jin, G. Popescu, N. Aluru, K. J. Hsia, and R. Bashir, "Measurement of adherent cell mass and growth," Proc. Natl. Acad. Sci. **107**, 20691–20696 (2010).
20. J. R. Fienup, "Phase retrieval algorithms: a comparison," Appl. optics **21**, 2758–2769 (1982).
21. S. Grilli, P. Ferraro, S. De Nicola, A. Finizio, G. Pierattini, and R. Meucci, "Whole optical wavefields reconstruction by digital holography," Opt. Express **9**, 294–302 (2001).
22. L. Herve, O. Cioni, P. Blandin, F. Navarro, M. Menneteau, T. Bordy, S. Morales, and C. Allier, "Multispectral total-variation reconstruction applied to lens-free microscopy," Biomed. Opt. Express **9**, 5828–5836 (2018).
23. M. R. Hestenes and E. Stiefel, *Methods of Conjugate Gradients for Solving Linear Systems*, vol. 49 (NBS Washington, DC, 1952).